Journal of Molecular Structure 1364 (2026) 145846

Contents lists available at ScienceDirect

Journal of Molecular Structure

journal homepage: www.elsevier.com/locate/molstr

Experimental and theoretical investigations of two novel benzhydrazones derived from 4-dimethylaminobenzhydrazide: Spectral, crystallographic, antibacterial and docking studies

P.R. Reshma [a,b,j], Lincy Tom [c], N.P. Dhanya [d,e], K.P. Safna Hussan [f,g], M.R.P. Kurup [h], V.B. Bhagyesh [i], Bibitha Joseph [a,j,*]

[a] Centre for Research in Chemical Sciences (CRCS), Department of Chemistry, St. Joseph's College (Autonomous), Irinjalakuda, Thrissur 680121, India
[b] Department of Chemistry, Govt. Engineering College, Thrissur 680009, Kerala, India
[c] Department of Chemistry, Nirmala College (Autonomous), Muvattupuzha, Ernakulam, 686661, Kerala, India
[d] Department of Physics, KKTM Govt. College Pullut, Thrissur 680663, Kerala, India
[e] Department of Physics, Christ College (Autonomous), Irinjalakuda, Thrissur 680125, India
[f] Ayurgreen Scientifica Research Institute LLP, Ayurgreen Campus, Kavilpadi, Kaladi, Malappuram, 679582, Kerala, India
[g] Micro/Nano Technology Centre, Tokai University, Hirastuka-Shi Kanagawa 259-1292, Japan
[h] Department of Chemistry, Central University of Kerala, Tejaswini Hills, Periye, Kasaragod 671 320, Kerala, India
[i] Department of Chemistry, Christ College (Autonomous), Irinjalakuda, Thrissur 680125, India
[j] University of Calicut, Thenhipalam, Malappuram 673635, Kerala, India

ARTICLE INFO

Keywords:
Benzhydrazone
4-dimethylaminobenzhydrazide
X-ray crystallography
DFT
Antibacterial activity
Molecular docking

ABSTRACT

Two novel benzhydrazone derivatives, **Hyet** (3-ethoxy salicylaldehyde 4-dimethylaminobenzhydrazone) and **Hybr** (3,5-dibromo salicylaldehyde 4-dimethylaminobenzhydrazone), were synthesized via condensation of 4-dimethylaminobenzhydrazide with substituted salicylaldehydes. Structural confirmation was achieved through ^{1}H NMR, FT-IR, UV–Vis, SCXRD, and elemental analysis. Single-crystal XRD revealed intermolecular hydrogen bonding as the primary stabilizing force in the crystal lattice. DFT (B3LYP/6–311G(d,p)) supported structural, vibrational, and electronic properties, with simulated NMR spectra aligning with experimental data. Frontier orbital analysis showed **Hyet** with stronger localized charge polarization, while **Hybr** exhibited a smaller HOMO–LUMO gap and higher electrophilicity, indicating greater global reactivity. Hirshfeld surface analysis highlighted key intermolecular interactions. Both compounds demonstrated notable antibacterial activity against Gram-positive and Gram-negative strains, further rationalized by molecular docking with bacterial target proteins.

1. Introduction

Aroylhydrazones formed through the condensation of aroylhydrazides with aldehydes or ketones exhibit remarkable conformational flexibility and versatile donor chemistry, making them one of the most intriguing subclasses of hydrazones [1–3]. Chemists can create ligands with adjustable properties because they are easy to synthesize and can be modified with different electron-donating or electron-withdrawing substituents. These ligands frequently function as bidentate donors by means of azomethine nitrogen and carbonyl oxygen; nevertheless, in the presence of additional donor atoms like hydroxyl group or heteroaromatic nitrogens, tridentate coordination is feasible [4]. These structural variations are extremely significant for their practical applications as well as their aesthetic and scholarly value. Their capacity to experience amido-iminol and keto-enol tautomerism is a crucial characteristic that improves their reactivity and coordination potential [5]. Their nucleophilic and electrophilic behaviour is enhanced by this tautomeric flexibility, which enables them to coordinate with a variety of metal ions in various oxidation states. Because of this adaptability and depending on the metal ion, ligand denticity, pH, and solvent system used, hydrazone-based ligands can form a wide range of monomeric, dimeric, oligomeric, and even polymeric complexes, with potential supramolecular architectures stabilized by metal–π interactions, π–π stacking, and hydrogen bonding [6–8].

* Corresponding author.
E-mail address: bibitha@stjosephs.edu.in (B. Joseph).

https://doi.org/10.1016/j.molstruc.2026.145846
Received 1 December 2025; Received in revised form 28 February 2026; Accepted 2 March 2026
Available online 3 March 2026

The ability of hydrazone metal complexes to stabilize different metal oxidation states and facilitate electron-transfer processes has led to a great deal of research on their role in catalysis, including electrocatalysis and photocatalysis [9,10]. Hydrazone ligands are molecular building blocks used in supramolecular chemistry that can be designed into large assemblies or frameworks for use in gas storage, magnetism, and sensing [11,12]. In medicinal chemistry and pharmaceutical research, hydrazones and their metal complexes play a crucial role, extending beyond coordination chemistry and materials science. Important pharmacological properties, including antimicrobial, antifungal, antiviral, anticancer, anti-inflammatory, antioxidant, antimalarial, anticonvulsant, and enzyme-inhibitory activities, have been shown by a variety of hydrazone derivatives and their metal complexes [13–16]. Metal coordination frequently improves pharmacokinetic parameters like solubility, stability, bioavailability, and cellular uptake, thereby increasing the therapeutic efficacy of these systems. Furthermore, the structural tunability of hydrazones enables the design of ligands with specific target affinity and reduced toxicity. The capacity of hydrazones to interact with biomolecular targets like DNA, proteins, and enzymes through intercalation, groove binding, or metal-mediated inhibition also affects their biological activities [17]. Hydrazones continue to be at the forefront of current research in inorganic, bioinorganic, and medicinal chemistry as scientists work to understand their intricate behaviour and diverse range of uses.

The aim of the present work is to synthesize and systematically characterize two novel benzhydrazone derivatives **Hyet** and **Hybr** derived from 4-dimethylaminobenzhydrazide using combined experimental and theoretical approaches. Particular emphasis is placed on elucidating their crystal structures. Hirshfeld surface analysis was used to visualize and measure intermolecular interactions within the crystal lattice [18], and density functional theory (DFT) calculations were used to investigate electronic properties. Antibacterial activity was evaluated against selected Gram-positive and Gram-negative bacterial strains. Molecular docking studies were further carried out to gain molecular-level insight into the antibacterial behaviour of the compounds [19].

2. Experimental

2.1. Materials and instrumentation

The reagents for synthesis were purchased from Merck, and the solvents were sourced from Aldrich Sigma Ltd. Elemental analyses for carbon, hydrogen, and nitrogen were performed using a Vario EL III elemental analyzer (Elementar). All spectroscopic measurements were carried out using recrystallized powdered samples unless otherwise stated. FT-IR spectra were recorded using a Shimadzu IR Spirit FTIR Spectrometer with DLATGS detector in the range of 4000–400 cm^{-1}, with a resolution of 4 cm^{-1} and 32 scans using the KBr pellet method. Thermo Scientific Evolution 201 UV–Vis double beam spectrophotometer was used to capture electronic spectra in the 200–800 nm region using 1×10^{-5} M DMF solutions. Proton nuclear magnetic resonance (^{1}H NMR) data was recorded in DMSO with TMS as internal standard using a Bruker Advance III 400 MHz spectrometer with a 9.4 T superconducting magnet.

2.2. General procedure for the synthesis of hydrazones

The two benzhydrazones were synthesized by using the method reported in previous literature [20].

2.2.1. Synthesis of 3-ethoxysalicylaldehyde 4-dimethylaminobenzhydrazone (Hyet)

A methanolic solution of 3-ethoxysalicylaldehyde (0.1661 g, 1 mmol) was added to a methanolic solution of 4-dimethylaminobenzhydrazide (0.1792 g, 1 mmol). Refluxing the reaction mixture for 4 h

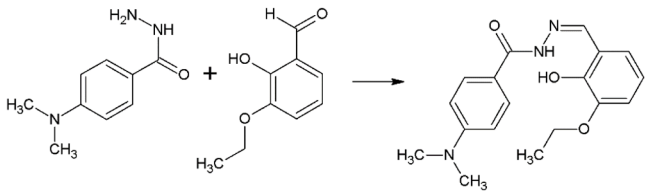

Scheme 1. Synthetic route for 3-ethoxy salicylaldehyde 4-dimethylaminobenzhydrazone (Hyet).

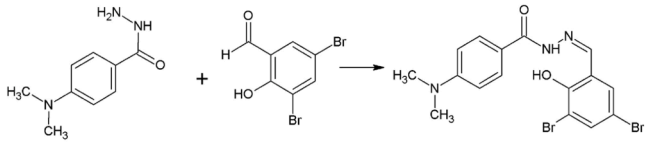

Scheme 2. Synthetic route for 3,5-dibromo salicylaldehyde 4-dimethylaminobenzhydrazone (Hybr).

followed by cooling led to the formation of yellow crystalline solids (Scheme 1). The precipitate was filtered, washed with methanol and air-dried. The crude product was further purified by recrystallization using a methanol/DMF mixture. Tiny block-shaped crystals suitable for single-crystal X-ray diffraction were obtained.

Yield: 83 %, M.P.: 190 °C; CHN calculated for $C_{18}H_{21}N_3O_3.H_2O$ (345.39): C, 62.59 %; H, 6.71 %; N, 12.17 %. Observed: C, 62.53 %; H, 6.73 %; N, 12.15 %.

2.2.2. Synthesis of 3,5 dibromosalicylaldehyde 4-dimethylaminobenzhydrazone (Hybr)

A methanolic solution of 3,5-dibromosalicylaldehyde (0.2799 g, 1 mmol) was added to a solution of 4-dimethylaminobenzhydrazide (0.1792 g, 1 mmol) in methanol. The mixture was refluxed for 4 h and then cooled, resulting in the formation of yellow solid. (Scheme 2) The solid was filtered off and washed with methanol. Recrystallization from a methanol/DMF mixture yielded pale yellow block-shaped crystals suitable for SCXRD.

Yield: 85 %, M.P.: 240 °C; CHN calculated for $C_{16}H_{15}Br_2N_3O_2$ (441.12): C, 43.56 %; H, 3.43 %; N, 9.53 %. Observed: C, 43.52 %; H, 3.39 %; N, 9.51 %.

2.3. X-ray analysis: Data collection, structure determination, and refinement

Crystallographic measurements were carried out on a Bruker SMART APEX diffractometer equipped with a graphite-monochromated MoKα radiation source (λ = 0.71073 Å). Data collection was performed using the Bruker SMART software suite, and integration of the diffraction data was completed with Bruker SAINT [21]. Absorption corrections were applied using SADABS based on Laue symmetry and equivalent reflections [22]. The structure was solved by direct methods with the SHELXL-97 package and refined against F^2 using full-matrix least-squares procedures [23,24]. All non-hydrogen atoms were refined anisotropically. Hydrogen atoms were identified from difference Fourier maps, positioned geometrically, and treated as riding atoms with fixed distances: C–*H* = 0.93 Å (heteroaromatic), 0.96 Å (CH_3), and N–*H* = 0.86–0.87 Å, with $U_{iso}(H) = 1.2\ U_{eq}(C, N)$. Bond lengths and angles were restrained using DFIX and DANG to preserve appropriate geometry. Molecular diagrams were prepared using DIAMOND 3.2 [25] software.

2.4. Computational procedure

All the quantum chemical calculations were conducted using density functional theory (DFT) and time dependent density functional theory

(TDDFT), utilizing Gaussian 09 software in gaseous phase [26]. The initial geometry of the compounds is collected from the crystal structure. Geometrical optimization was performed without applying symmetry constraints, utilizing 6311G(d,p) level of theory and basis set. Frequency analysis was executed using the same DFT level to validate the stability of the optimized molecular geometries [27]. The absence of negative frequency values affirms the stability of these optimized geometries. Frontier molecular orbitals (FMOs), UV/Vis spectra and molecular electrostatic potential (MEP) surface analysis at aforementioned basis set and level of theory were carried out using TDDFT calculations with B3LYP/6311G(d,p) method in DMF solution. GaussView version 6.0.16 were employed to interpret the data [28]. Simulated ^{1}H NMR spectra and predicted chemical shifts were generated using the Mnova NMR prediction module and compared with the experimental data [29].

2.5. Hirshfeld surface analysis and interaction energy calculations

Hirshfeld surface (HS) analysis is a potent technique for examining and visualizing the intermolecular interactions that support crystal structure stability [30]. Using the Crystal Explorer software (version-17.5) [31], which enables mapping of the crystal surface according to the normalized contact distance (d_{norm}), HS analysis was carried out in this study. This function takes into account the separation between the closest atoms inside (d_i) and outside (d_e) the molecular surface [32–34]. Red spots indicate regions where contacts are less than the sum of the van der Waals radii, whereas white and blue, respectively, indicate contacts that are equal to or greater than these distances [35]. Other surface characteristics, like curvedness and shape index, were also used to pinpoint particular supramolecular characteristics, such as hydrogen bonding interactions and π···π stacking. From the surfaces, two-dimensional fingerprint plots were produced, providing a numerical analysis of every kind of interaction and how it affects crystal packing. Additionally, HF/3–21 G level interaction energy calculations were performed to enhance comprehension of intermolecular forces [30]. To determine the total interaction energy (E_{tot}), these energies were broken down into electrostatic, polarization, dispersion, and exchange-repulsion components, and scaling factors were applied. These calculations shed light on the type and strength of intermolecular contacts in the crystal structures under study using a cluster of nearby molecules within a 3.8 Å radius.

2.6. in-vitro antibacterial studies

Antibacterial activity was carried out also by disc diffusion method [36] with some modifications. 0.1 ml of each bacterial culture (*Pseudomonas, Staphylococcus, E.coli, Bacillus*) was uniformly distributed on nutrient agar plates to prepare lawn culture. Sterile filter paper disc of 4 mm diameter was impregnated with varying concentrations of (20 µl of 0.1–10 mg/ml of dimethyl sulfoxide) and placed on the surface of nutrient agar plates at a distance of 2 cm using a sterile forceps. Disc with DMSO was used as control. The plates were incubated at 37 °C for 24 hrs and after incubation, zone diameter was measured.

2.7. Molecular docking procedure

Molecular docking is a widely used theoretical technique that predicts how a compound will bind to a protein or DNA, giving information about binding interactions, affinity, and the best location for the compound in drug design [37]. The RCSB Protein Data Bank provided the PDB IDs of the chosen target proteins, guaranteeing access to high-quality, experimentally resolved protein structures. Mercury software [38] was used to convert ligand structures from single-crystal X-ray diffraction (SXRD) data in CIF format to PDB format so that docking programs could use them. The Discovery Studio [39] was used to prepare the protein, which included a number of refinement processes like adding missing hydrogen atoms and removing heteroatoms and

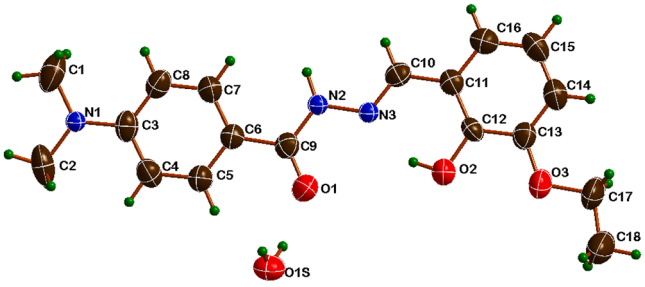

Fig. 1. A view of the molecular structure of Hyet, showing atom-numbering scheme for the asymmetric unit. Displacement ellipsoids are drawn at the 50 % probability level.

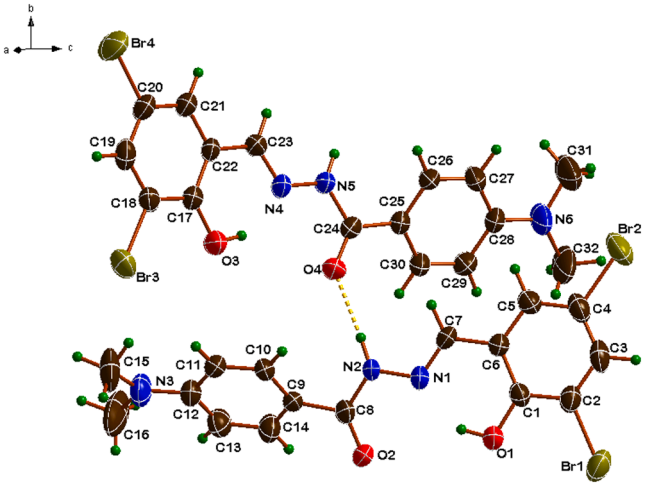

Fig. 2. A view of the molecular structure of Hybr, showing atom-numbering scheme for the asymmetric unit. Displacement ellipsoids are drawn at the 50 % probability level.

crystallographic water molecules. By taking this step, the protein was guaranteed to be in a stable and physiologically significant conformation for docking. After that, CB-Dock [40] was used for molecular docking, in which a cavity detection algorithm was used by the software to automatically identify the most likely binding pockets on the protein surface. It used flexible docking simulations to predict the ideal ligand orientation and conformation after ranking these pockets according to their size and suitability. Pose rankings were based on predicted stability, and binding affinity scores (Vina scores) were produced by the tool. After docking, interaction analysis was conducted once more using Discovery Studio. While 3D visualizations offered a realistic spatial understanding of the ligand's placement in the binding pocket, 2D interaction diagrams were produced to clearly depict hydrogen bonds, *π–π* stacking, *π*–alkyl interactions, hydrophobic contacts, and van der Waals forces. Accurate prediction and interpretation of ligand–protein interactions were guaranteed by this integrated workflow that included protein retrieval, ligand preparation, docking simulation, and thorough visualization.

3. Results and discussions

3.1. X-ray diffraction analysis

The crystal structures of **Hyet** and **Hybr** were elucidated by single crystal X-ray diffraction analysis. The compounds are structurally similar regarding the benzhydrazone moiety and differ in the salicylaldehyde moiety. The compound **Hyet** crystallizes with a solvent water molecule and was solved in the orthorhombic space group $P2_12_12_1$.

Table 1
Crystal and structure refinement data for compounds Hyet and Hybr.

Empirical formula	$C_{18}H_{21}N_3O_3.H_2O$ (Hyet)	$C_{16}H_{15}Br_2N_3O_2$ (Hybr)
Formula weight	345.39	441.13
Temperature	293(2) K	300(2) K
Wavelength	0.71073 Å	0.71073 Å
Space group	$P2_12_12_1$	*C2/c*
Crystal system	Orthorhombic	Monoclinic
Unit cell dimensions	a = 6.4444(14) Å *b* = 13.506(4) Å *c* = 20.846(5) Å	*a* = 22.318(3) Å *b* = 9.7910(12) Å *c* = 32.293(5) Å, β = 106.520(4)°
Volume	1814.4(8) $Å^3$	6765.2(16) $Å^3$
Z	4	16
Density (calculated)	1.264 mg/m^3	1.732 mg/m^3
Absorption coefficient	0.090 mm^{-1}	4.805 mm^{-1}
F(000)	736	3488
Reflections collected	14,921	65,203
Independent reflections	4347 [R(int) = 0.0671]	10,104 [R(int) = 0.1172]
Goodness-of-fit on F^2	0.923	0.984
Data / restraints / parameters	4347 / 5 / 242	8389 / 4/ 431
Final R indices [*I* > 2sigma(I)]	R_1= 0.0534 wR_2= 0.1003	R_1= 0.0542 wR_2= 0.0928

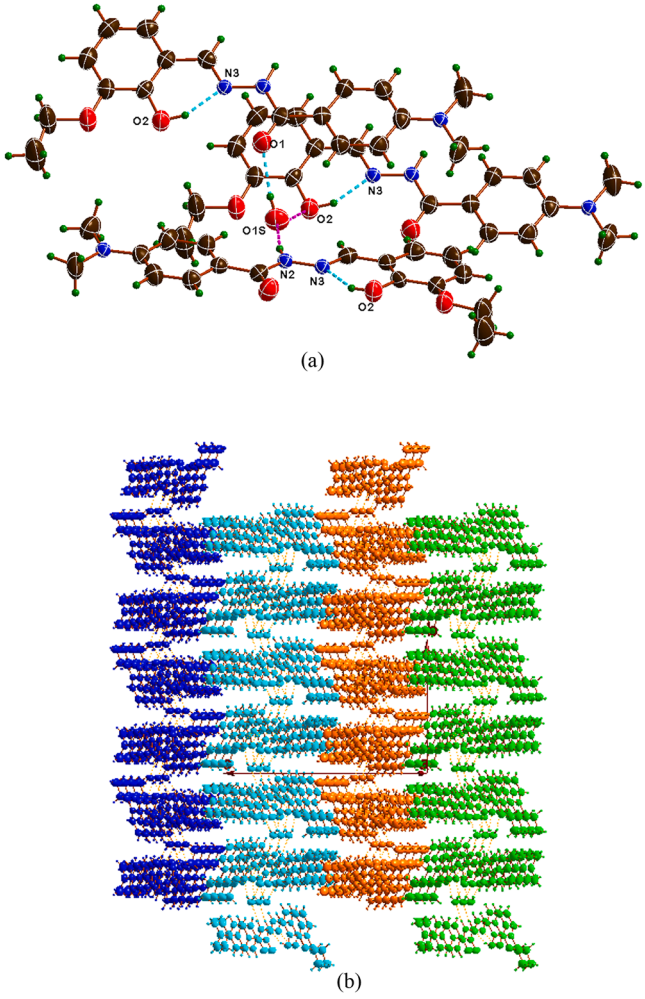

Fig. 3. (a) Intermolecular and intramolecular hydrogen bonding interactions in Hyet (b) 2D hydrogen bonded polymeric sheets of Hyet extending parallel to 'ab' (001) plane.

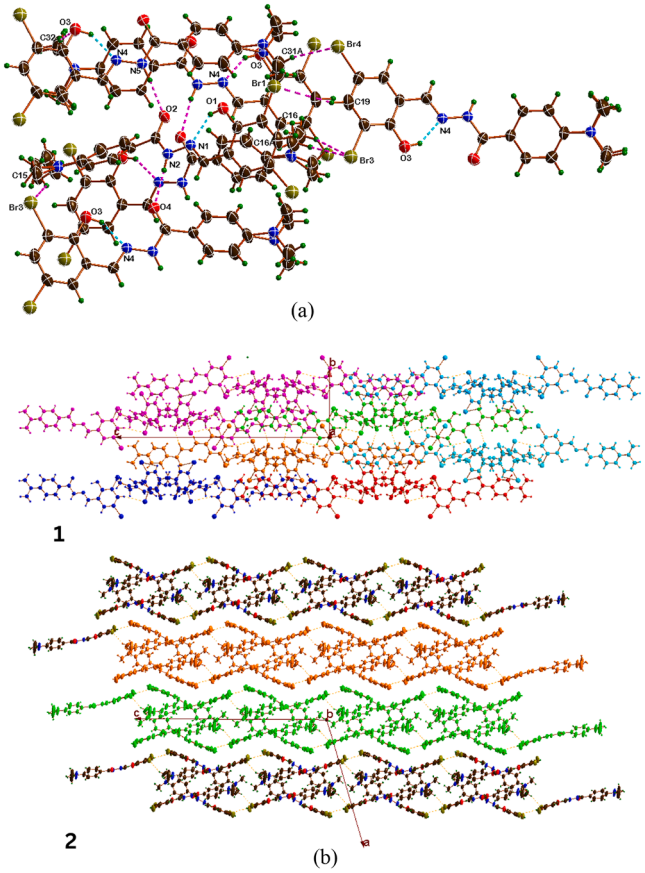

Fig. 4. (a) Intermolecular and intramolecular hydrogen bonding interactions in Hybr (b) 1D supramolecular chains (shown in different colours) parallel to the 'c' axis (2). The view of polymeric chain along 'a' axis. Molecular aggregates (shown in different colours) formed via C—H···Br contacts(1).

Whereas, asymmetric unit of **Hybr** comprises inverted dimers and crystallized in monoclinic space group *C2/c*.

Figs. 1 and 2 show the asymmetric unit and Table 1 represents the crystallographic parameters of compound **Hyet** and **Hybr**. The compounds adopt an *E* conformation around the double bond of the hydrazone bridge, and the observed *C* = *N* bond length (1.275(5) for both hydrazones) closely matches the formal azomethine linkage, thereby confirming the formation of the azomethine bond [41]. All other bond lengths and angles are within normal ranges and are comparable to those reported hydrazone compounds [42].

Classical and non-classical hydrogen-bonding interactions represent the main contributions to the packing of the molecules in the crystals of **Hyet** and **Hybr**. Numerical data are compiled in **Table S1**.

Hyet crystallizes as a hydrate, incorporating one lattice water molecule per asymmetric unit. The oxygen atom of the water molecule (O1S) plays a key structural role by functioning as both a hydrogen-bond donor and acceptor, thereby significantly contributing to the supramolecular assembly. As a donor, the water molecule forms intermolecular O–H···O hydrogen bonds with the hydroxyl group of a neighbouring molecule. In addition, the same water molecule participates as an acceptor in an intermolecular N(2)–H(2′)···O(1S) hydrogen bond involving a molecule located in the same crystallographic plane. Collectively, these O–H···O and N–H···O interactions link adjacent molecules into a two-dimensional hydrogen-bonded network parallel to the 'ab' (0 0 1) plane (Fig. 3), which serves as the primary motif governing the crystal packing of **Hyet.**

In **Hybr**, the dominant structure-directing forces are classical hydrogen bonds involving N–H donor. These hydrogen bonds link neighbouring molecules into continuous chains and form the backbone

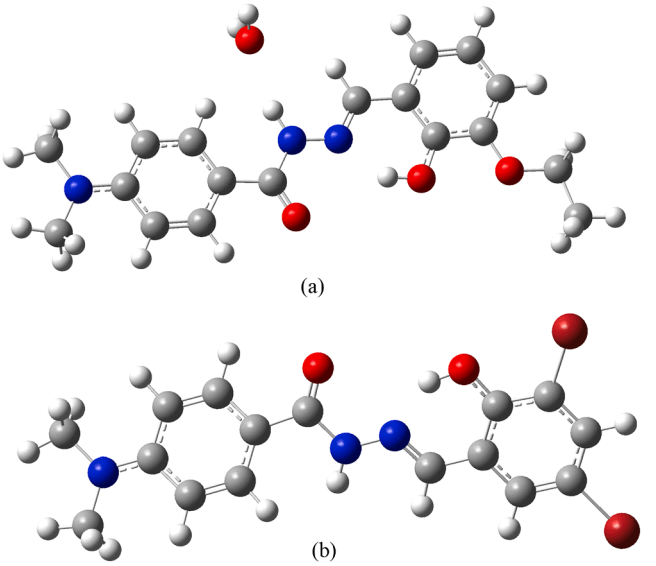

Fig. 5. Optimised structures of the prepared compounds (a) Hyet and (b) Hybr employing the DFT/B3LYP technique with the SDD and 6–311G(d,p) basis set.

of the crystal packing. Complementing the primary hydrogen-bonded motifs, weak non-classical C–H···Br interactions are present and lead to the formation of molecular aggregates rather than one-dimensional chains. These aggregates are subsequently cross-linked by N–H···O hydrogen-bonded chains, giving rise to an extended one-dimensional supramolecular architecture (Fig. 4).

In related hydrazone-based structures reported in the literature, intermolecular N–H···O hydrogen bonds between neighbouring hydrazone moieties are commonly observed and play a dominant role in stabilizing the crystal packing. In the present structure, however, the presence of a solvent molecule alters the hydrogen-bonding pattern, such that the N–H donor preferentially participates in hydrogen bonding with the solvent oxygen atom rather than forming direct N–H···O interactions between adjacent hydrazone units. Similar solvent-directed hydrogen-bonding behaviour has been reported for related systems, where inclusion of solvent molecules leads to modified supramolecular architectures [43–46].

3.2. Computational analysis

3.2.1. Optimized molecular structure

The optoelectronic properties of synthesized molecules were analysed using density functional theory to get more information on the molecular and electronic structures. The converged geometry was confirmed to be a true energy minimum by the absence of imaginary frequencies, indicating that the structure is stable and represents a genuine equilibrium configuration.

The optimized geometries are depicted in Fig. 5. The bond distances and angles in the optimized structures and the single-crystal structures are compared in **Table S2 and S3**. The geometrical parameters match those derived from X-ray diffraction measurements. XRD/DFT histogram of bond lengths and bond angles for compounds **Hyet** and **Hybr** is given in **Fig. S1. Hyet** exhibits markedly lower RMSD values of 0.0186 Å for bond lengths and 0.8608° for bond angles, indicating excellent agreement between experiment and theory and suggesting a more rigid molecular geometry with minimal packing-induced distortion. For **Hybr**, the bond-length and bond-angle RMSD values are 0.0579 Å and 3.0306°, respectively, indicating moderate deviations that can be attributed to crystal-packing effects, hydrogen-bonding interactions, and positional disorder present in the solid state. Overall, no significant differences are observed between the experimental and optimized geometrical parameters. The minor variations that do occur arise from the fact that the experimental structure corresponds to the crystalline phase, whereas the theoretical geometry represents an isolated molecule in the gas phase, where packing effects and intermolecular interactions are absent.

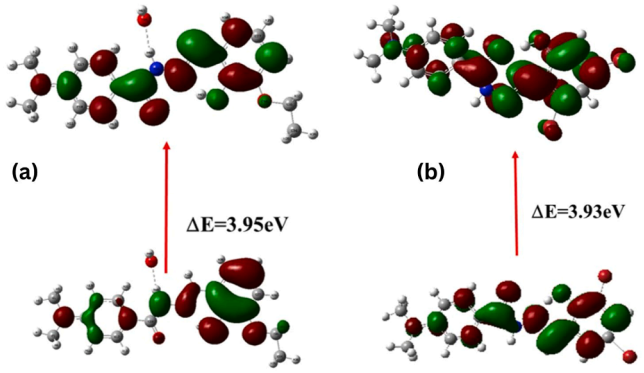

Fig. 6. HOMO and LUMO with bandgap energies in respect of compounds (a) Hyet and (b) Hybr.

3.2.2. Frontier molecular orbitals (FMOs) analysis

Frontier molecular orbitals (FMOs) play a key role in determining the chemical stability of a molecule and are highly useful for understanding properties such as electronic transitions, optical behaviour, and biological activity. Among these orbitals, the highest occupied molecular orbital (HOMO) and the lowest unoccupied molecular orbital (LUMO) are particularly significant. The energy gap between HOMO and LUMO provides an indication of the molecule's chemical stability [37].

The bonding characteristics of the studied molecules can be interpreted through the visualization of their FMO surfaces. A molecules signature quantities like hardness, softness, dynamic stability, electronegativity and reactivity can be interpreted using FMO analysis [47]. The HOMO energy marks the nucleophilic potential and LUMO energy denotes the electrophilic potential of a molecule The energy difference between the highest occupied molecular orbital (HOMO) and the lowest unoccupied molecular orbital (LUMO) is denoted as E_{gap} [48]. Highest chemical stability, less reactivity and higher hardness of a molecule will be the sign of higher E_{gap} value [49]. While a soft molecule is characterized by a smaller energy gap, with higher reactivity and less stability [50]. To get insight the optical properties of the compounds the FMOs energies and their respective band gap values were calculated via DFT employing 6–311 G (d, p) functional. HOMO and LUMO orbital transitions were scattered on phenyl ring, $C = N$, $C = O$ and $C - N$ groups and dispersion of the atoms is similar for the ligands.

The computed HOMO-LUMO energy gaps were 3.95 and 3.93 eV respectively for **Hyet** and **Hybr**. The **Hybr** molecule's relatively small energy gap (3.93 eV) suggests greater chemical reactivity, reduced dynamic stability, increased softness, and higher polarizability, indicating that charge transfer between the HOMO and LUMO occurs more readily. The HOMO and LUMO of compound **Hyet** and **Hybr** are shown in Fig. 6.

3.2.3. Global reactivity descriptors (GRDs)

The chemical reactivity and stability of synthesized compounds can be effectively elucidated with global reactivity descriptors (GRDs) computed by utilizing the FMOs energy gaps [51]. The factors electron affinity (EA), ionization potential (IP), global hardness (η), electrophilicity index (ω), electronegativity (X) chemical potential (μ), and global softness (σ) describes the reactivity of the molecules [52,53]. Based on Koopmans's theorem these parameters can be estimated. Electron affinity (EA) and ionization potential (IP) have taken as EA = $-E_{LUMO}$ and IP = $-E_{HOMO}$, electronegativity (χ) = (IP+EA)/2, chemical potential (μ) = -(IP+EA)/2, chemical hardness (η) = (- IP-EA)/2, chemical softness (σ) = 1/2η, electrophilicity index (ω) = $\mu^2/2\,\eta$. The calculated global

Table 2
Calculated electronic parameters of the two compounds using DFT/B3LYP/6311G(d,p) level of theory.

Global descriptive parameter	Calculated values	
	Hyet	Hybr
E HOMO (eV)	−5.22	−5.53
E LUMO (eV)	−1.28	−1.6
Band Gap energy (eV)	3.95	3.93
Ionisation Potential (IP)	5.22	5.53
Electron Affinity (EA)	1.28	1.6
Hardness (η)	1.97	1.96
Softness (S)	0.25	0.25
Electronegativity (χ)	3.25	3.56
Chemical potential (μ)	−3.25	−3.56
Electrophilicity index (ω)	2.71	3.29

descriptive parameters are given in Table 2.

The electrophilicity index (ω) evaluates a compound's electrophilic nature, offering useful information about its reactivity and interaction patterns. It is especially helpful in predicting potential toxicity and biological activity. Organic compounds can be grouped into three categories based on their electrophilicity index: marginal electrophiles (<0.8 eV), moderate electrophiles (0.8–1.5 eV), and strong electrophiles (greater than 1.5 eV). Accordingly, the electrophilicity values of our hydrazones place them in the strong electrophile category. It is clear that the high electrophilicity (5.06 eV) and small chemical hardness (1.87 eV) correspond to high absolute value of chemical potential (4.35 eV) for compound **Hyet** thereby, suggesting more biological activities for compound **Hyet** compared to **Hybr**.

3.2.4. *Molecular electrostatic potential (MEP)*

MEP maps help us to observe the charge distributions of molecules in three dimensions. Hydrogen bonding sites and the sites susceptible for electrophilic, nucleophilic reactions can be studied using charge distributions. MEP provides visual information about electronegativity, partial charges, and, dipole moment and the polarity of a structure. The MEP calculation surface of the compounds is shown in **Fig. S2**, negative (red or yellow) regions of MEP indicate electrophilic reactivity, be associated with electronegative atoms (O, N, halogens) while positive (blue) regions represent nucleophilic reactivity and are present near hydrogen atoms attached to electronegative atoms. The dispersion of potential in **Hyet** range from −9.101 e-3 to 9.101 e-3, and where as in **Hybr** is −5.862 e-3 to 5.862 e-3. This wider dispersion in **Hyet** indicates a more pronounced charge polarization, suggesting higher reactivity. In contrast, the narrower range in **Hybr** reflects a less polarized charge distribution, implying comparatively lower reactivity.

3.3. *Spectral analysis*

3.3.1. *FT-IR and electronic spectral analysis*

The experimental and calculated FT-IR spectra of **Hyet** and **Hybr** are presented in Fig. 7. Optimized structure parameters are used to find the vibrational frequencies of the hydrazones and the theoretical spectrum is developed using TD-SCF DFT-B3LYP/6–311G(d,p). The comparison of experimental and theoretical frequencies and their tentative assignments of the important bands of the two compounds are detailed in **Table S4**. It is observed that a good level of agreement has been achieved between the experimental spectrum and the theoretically calculated one. The slight differences observed between the experimental and theoretical results can be attributed to anharmonic effects, intermolecular interactions, and hydrogen bonding present in the solid state but absent in the isolated-molecule calculations [54].

In both compounds, the N–H stretching vibration appears as a weak band in the high-frequency region. For **HyEt**, the ν(N–H) band is observed at 3358 cm^{-1}, while **HyBr** shows a corresponding band at **3643** cm^{-1}, in good agreement with the calculated frequencies at 3426 and 3531 cm^{-1}, respectively [55]. The O–H stretching vibration appears at 3227 cm^{-1} for **HyEt** and at 3320 cm^{-1} for **HyBr**, consistent with the computed values and indicative of hydrogen-bonded hydroxyl groups. **In HyEt**, additional bands observed at 3544 cm^{-1} are assigned to the symmetric and asymmetric stretching modes of lattice water, supported by the calculated frequencies. The aromatic C–H stretching vibrations are observed in the region 3120 cm^{-1} for **HyEt** and around 3067 cm^{-1} for **HyBr**, matching well with the theoretical predictions. Aliphatic C–H stretching modes arising from the N–CH_3 and CH_2/CH_3 groups appear in the range 2948–2823 cm^{-1} for **HyEt** and 3006–2913 cm^{-1} for **HyBr**, in close correspondence with the calculated values [56].

Strong bands observed at 1736–1673 cm^{-1} for **HyEt** and at 1684 cm^{-1} for **HyBr** are assigned to the combined ν(C = O) and ν(C = N) stretching modes of the hydrazone moiety, confirming the formation of the azomethine linkage [57]. The aromatic C = C stretching vibrations appear prominently between 1602 and 1555 cm^{-1} in the experimental spectra and are well reproduced in the calculated spectra. Bands in the region 1285–1170 cm^{-1} are attributed to ν(C–N) and ν(C–O) stretching modes, further confirming the structural integrity of the hydrazone framework. The lower-frequency region (1150–800 cm^{-1}) is dominated by ring-puckering vibrations and out-of-plane C–H bending modes, which are well supported by the calculated spectra [58]. For **HyBr**, a characteristic band observed at 677 cm^{-1} is assigned to the ν(C–Br) stretching vibration, in good agreement with the theoretical value at 692 cm^{-1}, confirming the presence of bromine substituents in the molecular structure. The RMSD value for **Hyet** (67.37 cm^{-1}) and **Hybr** (54.52 cm^{-1}) confirms the validity of the theoretical approach for these compounds by

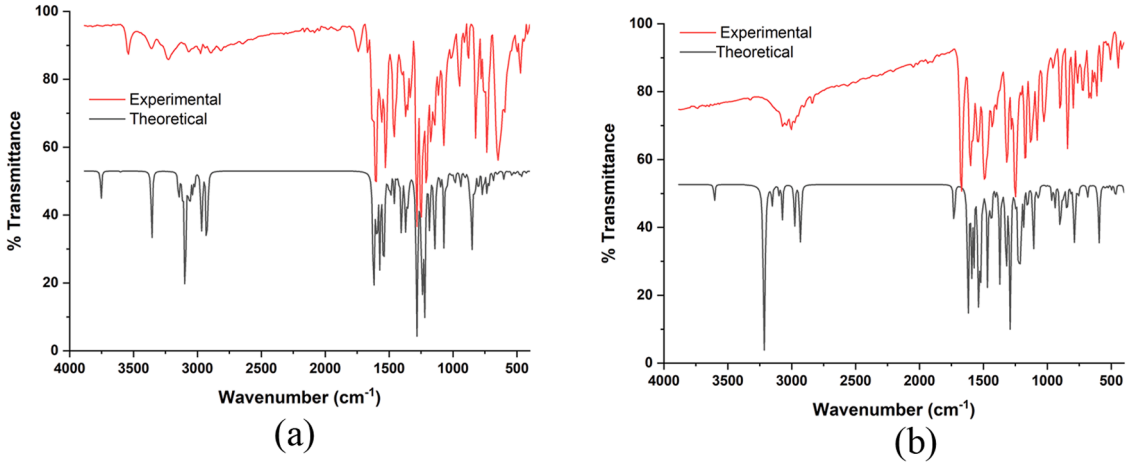

Fig. 7. Experimental and theoretical FT-IR spectra of Hyet (a) and Hybr (b).

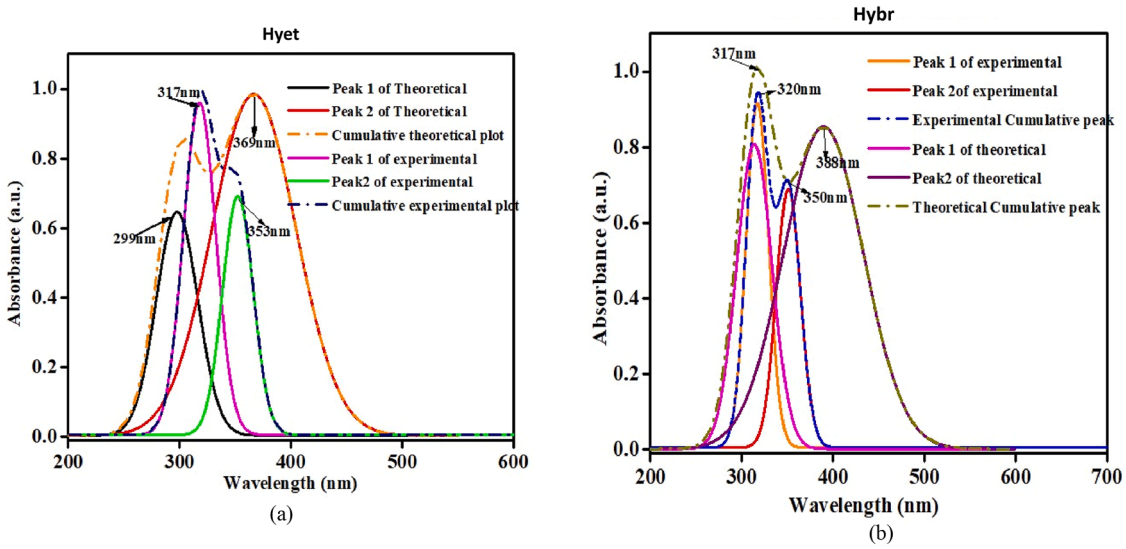

Fig. 8. Theoretical and experimental UV–Vis spectra of (a) Hyet and (b) Hybr.

showing good agreement between calculated and experimental IR frequencies.

The UV–Vis spectra of both hydrazone derivatives were experimentally recorded in DMF and compared with the corresponding theoretical predictions obtained using TD-SCF DFT at the B3LYP/6–311G(d,p) level, as shown in Fig. 8. The calculated spectra consist of discrete electronic transitions, which appear as individual peaks and correspond to specific excitations. In contrast, the experimental spectra represent broadened absorption bands arising from the cumulative contribution of multiple electronic transitions, influenced by solvent effects, vibrational coupling and instrumental broadening.

For **HyEt**, the experimental spectrum exhibits two absorption bands. The band centered around 353 nm is assigned to a π→π* transition originating from the aromatic moieties of the molecule, while a weaker band at 369 nm is attributed to an n→π* transition. The TD-DFT calculations reproduce this pattern, with corresponding transitions appearing at 299 nm (π→π*) and 317 nm (n→π*), respectively. Similarly, **HyBr** shows good agreement between the experimental and theoretical spectra. The π→π* transition appears at 317 nm in the theoretical spectrum and at 320 nm in the experimental spectrum, indicating excellent correlation. The n→π* transition, however, shows a noticeable red shift in the experimental spectrum relative to the theoretical prediction, which can be attributed to solvent effects in DMF that are not fully captured in the gas-phase calculations.

3.3.2. ^{1}H NMR spectral analysis

Nuclear Magnetic Resonance (NMR) spectroscopy has become the dominant method of analysis for organic compounds because in many cases it provides a way to determine an entire structure using one set of analytical tests. The ^{1}HNMR and ^{13}CNMR spectra of **Hyet** and **Hybr** were recorded using DMSO as the solvent and processed with MestReNova (Mnova). (**Fig. S3, S4, S5** and **S6**). Two broad resonances at δ 11.81 and 11.29 ppm in the experimental ^{1}H NMR spectrum of **Hyet** are attributed to phenolic -OH protons and iminol protons respectively confirming that the hydrazone exists predominantly in the iminol form in solution. In **Hybr** these peaks are appeared by two downfield singlets at δ12.9 and 12.2 ppm respectively. These resonances are not present in the Mnova simulated spectrum, which could be because solvent and hydrogen-bonding effects were not included in the calculations. In **Hyet** the azomethine proton is well predicted by Mnova at δ 8.34 ppm and appears at δ 8.59 ppm in experiments. The calculated range of δ 6.82–7.85 ppm is closely matched by the resonance of aromatic protons in the range δ 6.74–7.82 ppm [11]. The peaks, particularly the azomethine, aromatic, and N-methyl protons, of **Hybr** show good agreement between experimental and simulated chemical shifts, supporting the proposed molecular structure. In ^{13}CNMR spectra of both compounds, the imine carbon appears prominently at δ 163 ppm, slightly upfield compared to the theoretical values (δ 170 ppm), which can be attributed to solvent effects and electronic shielding. Azomethine carbon and aromatic carbons linked to oxygen and nitrogen resonate around δ150 ppm in experimental and simulated spectra. The aliphatic methylene carbon (–CH_2–) in **Hyet** is observed at δ 64.6 ppm, in close agreement with the theoretical value, while the dimethylamino carbon –$N(CH_3)_2$ resonates at δ 40 ppm in both compounds. The RMSD values for the ^{1}H NMR spectra, excluding exchangeable –OH protons, are 0.1168 ppm for **Hyet** and 0.0684 ppm for **Hybr**, while the corresponding ^{13}C NMR RMSD values are 2.82 ppm and 4.96 ppm, respectively. (**Table S5**).

3.4. Hirshfeld surface analysis

The surface can be mapped over parameters like d_{norm}, shape index, and curvedness to differentiate between different types of interactions, such as halogen contacts, hydrogen bonds, van der Waals forces, and π–π stacking. By using this technique, the internal (d_i) and external (d_e) atomic distances can be measured and a molecular boundary similar to van der Waals surfaces is defined. The X-ray structure of the two hydrazones was examined using Hirshfeld surface analysis in order to identify the main interactions influencing the stability of crystal packing. It was determined that the values of total volume, area, globularity, and sphericity were 445.02Å^3, 420.07 Å^2, 0.671 and 0.439 for **Hyet** and 410.68Å^3, 376.61Å^2, 0.709 and 0.432 for **Hybr**. Globularity <1.0, suggesting a more ordered surface with some degree of anisotropy and deviations from perfect sphericity. The molecular structure and the spatial distribution of interaction properties are clearly depicted by the Hirshfeld surface, which is mapped over d_{norm}, shape index and curvedness in a transparent mode **(Fig.S7).** Large, deep-red circular areas on the d_{norm}-mapped surface indicate strong, short-range intermolecular hydrogen bonds, while smaller, lighter-colored spots represent weaker, longer-range contacts that go beyond hydrogen bonds. Regions of strong molecular interactions are indicated by these red depressions, particularly H···N and H···O contacts that result from O–H···N and N–H···O hydrogen bonding patterns [59]. The Hirshfeld surface analysis is in good agreement with the single-crystal X-ray diffraction results. The prominent red regions on the d_{norm} surface correspond to the same O–H···N and N–H···O hydrogen bonds identified crystallographically,

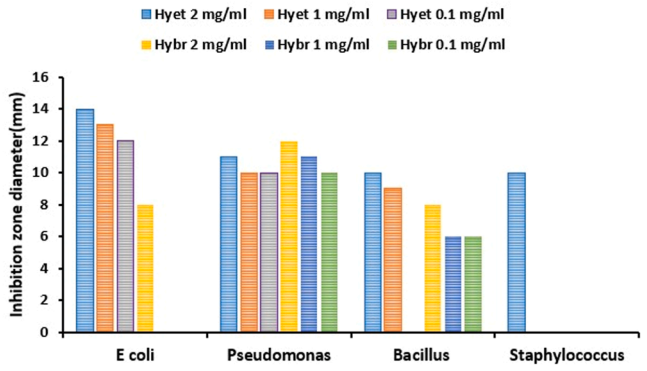

Fig. 9. Graphical representation of antibacterial activity of Hyet and Hybr.

confirming that these interactions dominate the crystal packing. The presence of flat regions on the curvedness surface further supports the presence of weak aromatic π–π stacking interactions, which are characterized by distinct red concave regions on the shape-index surface.

As a reduced form of the 3D surface, the 2D fingerprint plots for the two compounds, which are produced by combining the Hirshfeld surface parameters d_i and d_e into 0.01 Å intervals, show the type, nature, and importance of all intermolecular interactions in the crystal lattice as well as their individual contributions to the total Hirshfeld surface area, as seen in The 2D fingerprint plot analysis (**Fig. S8**) of **Hyet** reveals that H···H contacts account for 55.8 % of the Hirshfeld surface, with C–H/H–C interactions coming in second at 17.3 % and H–O/O–H interactions at 17.3 %. Van der Waals forces and hydrogen bonding are important factors in the crystal packing, as evidenced by the smaller contributions from the C–N/N–C (4 %), C–C (3.2 %), N–H/H–N (1.3 %), C–O/O–C (0.9 %) and O–O (0.1 %) contacts. The 2D fingerprint plot for **Hybr** shows that H···H contacts account for the largest portion of the Hirshfeld surface at 30.5 %, followed by Br–H/H–Br contacts (20.3 %) and H–C/C–H interactions (21.8 %) (**Fig. S9**). Significant contributions also come from O–H/H–O interactions (14.2 %), while H–N/N–H contacts account for 3.7 %. Smaller contributions are observed for Br–Br (3.5 %), Br–O/O–Br (1.1 %), Br–N/N–Br (1.9 %), Br–C/C–Br (1 %), O–C/C–O (0.7 %), and N–C/C–N (0.5 %) interactions. These observations highlight the influence of both hydrogen bonding and halogen interactions in the crystal packing, as clearly evidenced by the single-crystal X-ray diffraction analysis. The symmetry-independent molecules in each cluster are represented by red, green, and blue cylinders, which stand for $E_{ele}c$, E_{dis}, and E_{t_ot}, respectively (**Fig. S10**). The frameworks are constructed by connecting molecular pair-wise interaction energies to molecular centroids with cylinders whose radii match the interaction. The total interaction energy (E_{tot}) is obtained as the sum of the electrostatic, polarization, dispersion, and repulsion energy components (**Fig. S11** and **S12**).

3.5. *In vitro antibacterial activity*

The *in vitro* antibacterial activity of the two synthesized hydrazones was studied against both Gram-positive (*Staphylococcus aureus, Bacillus sp.*) and Gram-negative (*E. coli, Pseudomonas sp.*) bacteria by employing the disc diffusion method [36]. The inhibition zone measurements obtained which indicate the relative antibacterial strength of each compound, are shown in **Table S6**. The results show clear differences in antibacterial responsiveness. The strongest inhibitory effect against *E. coli* was shown by **Hyet. Hybr** showed better activity against *Pseudomonas* than *E.coli*. Additionally, the progressive enlargement of inhibition zones showed that the compounds' activity increased steadily with concentration, suggesting stronger bacterial suppression at higher doses. At the 3 mg/mL **Hyet** formed a 15 mm inhibition zone against *E. coli*, whereas **Hybr** produced a 12 mm zone against *Pseudomonas* (**Fig. S13**).

Table 3
Interactions of hydrazones with the amino acid residues of the target protein LAF6 in *E.coli* and 6R3X in *Pseudomonas aeruginosa.*

Ligand	Target (PDB)	Binding Score (kcal/mol)	H-Bond Residues (distance Å)	π–π / π-Alkyl Residues	Van der Waals Residues
Hyet	*E. coli* 1AF6	−8.7	ASP116 (2.68), HIS113 (2.16), TYR118 (2.09)	π–π: TYR41, TRP420; π-alkyl: TRP358	TYR6, ARG8, ARG33, ARG82, ARG109, GLU43, ASP11, HIS113
Hybr	*Pseudomonas aeruginosa* 6R3X	−8.8	ARG331 (2.27), THR487 (2.38), ASN351 (2.20, 2.70)	π–π: TYR409, PHE533; π-alkyl: TYR328, TYR407, TYR498, VAL333	ILE330, THR329, SER294, SER349, ALA488, GLY486, GLY534, GLY535, ARG489

Minimal inhibitory effects against Bacillus were shown by both **Hyet** and **Hybr. Hyet** displayed slight activity toward *S. aureus*, but only at high concentrations, while **Hybr** did not exhibit any discernible activity against *S. aureus*. The antibacterial activity of the two benzhydrazones is compared graphically in Fig. 9.

3.6. *Molecular docking analysis*

In vitro antibacterial studies revealed that **Hyet** exhibited the highest activity against *E. coli*, whereas **Hybr** was most effective against *Pseudomonas* species. Following these results, molecular docking studies were performed against five structural proteins of the respective organisms. The protein–compound complex with the highest docking score was then selected for an in-depth analysis (Table 3). In molecular docking, the stability of a ligand–protein complex is governed by a variety of non-covalent interactions, including hydrogen bonding, hydrophobic effects, van der Waals forces, electrostatic attractions, and π-related interactions such as π–π stacking and aromatic packing. These complementary forces not only anchor the ligand within the protein's active site but also influence its binding affinity, specificity, and overall docking score. By shaping both the strength and selectivity of the interaction, they play a critical role in determining the predicted biological activity and functional relevance of the complex.

Five structural proteins, denoted by the PDB IDs 1AF6, 1BXW, 2YIB, 3SLJ, and 2HDF, were selected for the docking analysis of **Hyet** against *E. coli*. 1AF6 showed the strongest binding interaction, as indicated by the obtained docking scores of −8.7, −8.3, −8.1, −7.8, and −7.7, respectively. The binding pocket of this protein measured 25 × 25 × 25 Å and had a cavity volume of 760. Its center was located at coordinates (19,42,80). 1AF6, also referred to as LamB or maltoporin, is an essential porin of the *E. coli* outer membrane that creates channels for the specific movement of sugars like maltose and maltodextrins. It is an embedded structural protein that aids in the passage of particular molecules while preserving the integrity of the membrane. 2D and 3D plots of 1AF6 with **Hyet** are shown in Fig. 10. ASP116 at 2.68 Å, HIS113 at 2.16 Å, and TYR118 at 2.09 Å were the three conventional hydrogen bonds identified by the docking analysis. There were π–alkyl interactions involving TRP358 and π–π stacking interactions with TYR41 and TRP420. The following were observed to have van der Waals interactions: TYR6, ARG33, ARG109, GLU43, ARG8, ARG82, and ASP11. An unfavourable donor-donor interaction between HIS113 and the OH group's hydrogen atom was also present.

For the docking study with **Hybr**, the PDB IDs 6R3X, 4O0P, 6JAU,

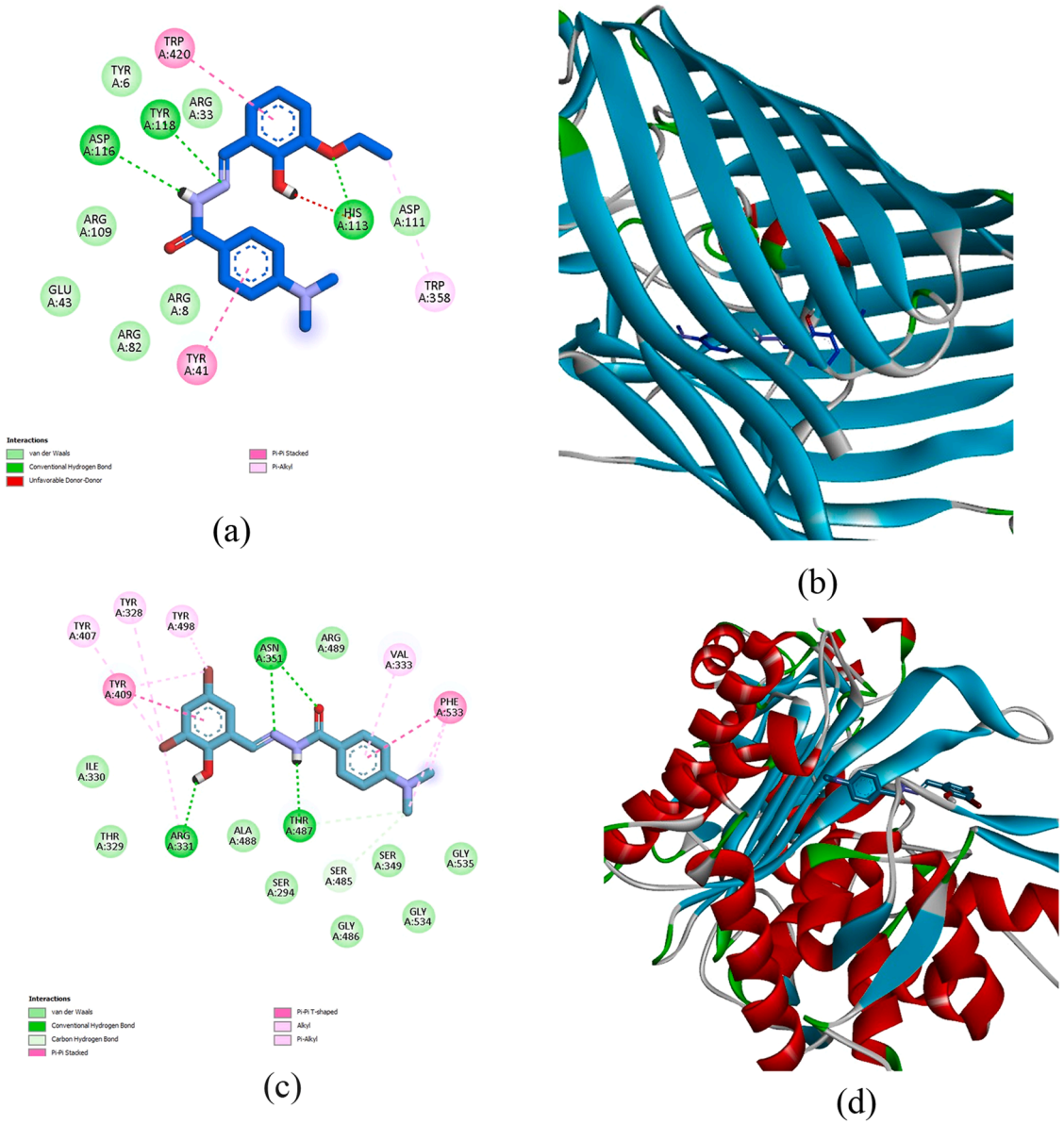

Fig. 10. 2D and 3D interaction diagram of (a and b) Hyet with 1AF6 and (c and d) HyBr with 6R3X.

7WL, and 6P8U were chosen as the structural protein targets of Pseudomonas. Their respective docking scores were −8.8, −8.6, −8.2, −8.2 and −7.9 kcal/mol, with 6R3X showing the highest binding affinity. The 6R3X binding site had a grid box size of 30 × 24 × 24 Å, a cavity volume of 1402, and a center at coordinates (4,40,19). Pseudomonas aeruginosa Penicillin-Binding Protein 3 (PBP3), a transpeptidase enzyme that catalyzes the crosslinking of peptidoglycan strands during the last phases of cell wall synthesis, is identified by the PDB entry 6R3X. Bacterial cell death is the ultimate result of β-lactam antibiotics like piperacillin inhibiting PBP3, which stops cell wall biosynthesis. Fig. 10 depicts the 2D and 3D plot of 6R3X with **Hybr.** Four typical hydrogen bonds were found for the 6r3x–Hybr complex: two contacts with ASN351 (2.20 Å and 2.70 Å), THR487 (2.38 Å), and ARG331 (2.27 Å). TYR409 and PHE533 engaged in π–π stacking, whereas SER485 formed a single C–H bond. There were π–alkyl interactions with VAL333, TYR407, TYR328, and TYR498. ILE330, THR329, ALA488, SER294, SER349, GLY535, GLY486, GLY534, and ARG489 were among the residues that helped bind *via* van der Waals forces. The detailed interactions of the two studied compounds with the respective proteins are shown in **Fig S14.**

3.7. ADME analysis

In order to forecast a compound's drug-likeness and pharmacokinetic behavior, ADME analysis evaluates its absorption, distribution, metabolism, and excretion. **Hyet** has better drug-like properties than the brominated derivative **Hybr**, according to a comparative ADME analysis of the two hydrazone derivatives. While **Hybr** is heavier (441.12 g/mol) and more lipophilic (log P = 3.55), which results in decreased aqueous solubility, the first compound has a lower molecular weight (327.38 g/mol) and moderate lipophilicity (log P = 2.83), which contribute to better solubility and membrane permeability. Both substances show similar CYP enzyme inhibition profiles (CYP1A2, CYP2C19, and CYP2C9), high gastrointestinal absorption, and blood–brain barrier permeability, suggesting similar metabolic behaviour. However, **Hyet** is better suited for oral bioavailability and pharmacokinetic stability due to its higher solubility and fewer rule violations. While **Hybr** may have a stronger binding potential due to its increased lipophilicity but decreased solubility, **Hyet** generally shows a better balance of pharmacokinetic and physicochemical properties.

The physicochemical balance of the two hydrazone derivatives is

Table 4
Lipinski rule of five-In silico physicochemical and pharmacokinetic parameters of the synthesized hydrazones.

Hydrazone	log P <5	MW <500 g/mol	H-Bond acceptor <10	H-Bond donor <5	n-rot	TPSA (°A)	Molar refractivity 40–130
Hyet	2.83	327.38	4	2	7	74.16	95.14
Hybr	3.55	441.12	3	2	5	64.93	99.24

clearly different, as shown by their radar plots. With moderate lipophilicity, polarity, solubility, and flexibility values, Hyet exhibits a more homogeneous and evenly distributed radar shape, indicating a good balance between hydrophobicity and hydrophilicity—perfect for oral drug candidates. Hybr, on the other hand, exhibits a wider area in the size (SIZE) and lipophilicity (LIPO) regions, but a narrower spread in the solubility (INSOLU) and saturation (INSATU) regions, suggesting that it is less flexible and soluble but more lipophilic and larger (**Fig. S15**). Its greater molecular weight and decreased solubility in comparison to the first compound are reflected in this pattern. Although **Hybr** may be more effective in hydrophobic interactions, the radar plot comparison suggests that **Hyet** has a better balance between drug-likeness and absorption, while **Hybr** may struggle with formulation and solubility. Because both hydrazone derivatives have acceptable molecular weight, lipophilicity, hydrogen bond donors, and acceptors within the suggested ranges (Table 4), they meet Lipinski's rule of five [60], indicating good oral drug-likeness.

4. Conclusion

Two new benzhydrazones were synthesized by condensing 4-dimethylaminobenzhydrazide with 3-ethoxysalicylaldehyde and 3,5-dibromosalicylaldehyde: 3-ethoxysalicylaldehyde-4-dimethylaminobenzhy drazone (**Hyet**) and 3,5-dibromo salicylaldehyde-4-dimethyla minobenzhydrazone (**Hybr**). A combination of physicochemical techniques confirmed their formation and structural features. Hydrogen-bonding and the overall supramolecular architecture were found to be significantly impacted by modifications to the substituents on the hydrazone backbone. Single-crystal X-ray diffraction provided accurate three-dimensional molecular structures, revealed distinct hydrogen-bonding motifs, and established that the crystal packing is governed by one-dimensional and two dimesional supramolecular architectures arising from specific intermolecular interactions. Density functional theory calculations further elucidated the optimized geometries and electronic properties of the isolated molecules and showed good qualitative agreement with experimental observations. Global reactivity descriptors indicate that **HyBr,** with its lower energy gap and higher electron-accepting capability, is more electrophilic and chemically reactive, whereas **HyEt** exhibits slightly higher hardness and resistance to charge transfer. Hirshfeld surface analysis was used to better understand solid-state interactions by identifying and visualizing the important intermolecular contacts, including H···H, O···H, C···H, and halogen-associated interactions that affect crystal packing and lattice stability. Both hydrazones have significant antibacterial activity, according to biological screening; **Hyet** was most effective against *E. coli*, while **Hybr** was more effective against *Pseudomonas* species. Molecular docking studies were performed against four target proteins from each bacterium in order to interpret these findings. **Hybr** showed its strongest interaction (–8.8 kcal/mol) with the 6R3X protein, while *Hyet* obtained its best binding score (–8.7 kcal/mol) with the 1AF6 protein. **Hyet** shows slightly better oral bioavailability potential than **Hybr** although both satisfy Lipinski's criteria and fall within acceptable bioavailability ranges.

CRediT authorship contribution statement

P.R. Reshma: Writing – original draft. **Lincy Tom:** Writing – original draft. **N.P. Dhanya:** Writing – original draft, Software. **K.P. Safna Hussan:** Writing – original draft, Software. **M.R.P. Kurup:** Formal analysis. **V.B. Bhagyesh:** Writing – original draft. **Bibitha Joseph:** Supervision.

Declaration of competing interest

The authors declare that they have no known competing financial interests or personal relationships that could have appeared to influence the work reported in this paper.

Acknowledgements

Bibitha Joseph and P.R. Reshma acknowledge DST-FIST (SR/FST/College-001/2009(c) and SR/FST/COLLEGE/2023/1354), DST-CURIE (DST/CURIE-PG/2023/33) and KSCSTE-SARD (KSCSTE/623/2019-SARD) support to St Joseph's College (Autonomous), Irinjalakuda. The authors are grateful to SAIF, Cochin University of Science and Technology, Kochi, Kerala, India for elemental analysis and Single Crystal X-ray diffraction studies.

Supplementary materials

Supplementary material associated with this article can be found, in the online version, at doi:10.1016/j.molstruc.2026.145846.

Appendix A. Supplementary data

CCDC 2512010 and 2512,011 contains the supplementary crystallographic data for compounds Hyet and Hybr respectively. Copies of this information may be obtained free of charge via www.ccdc.cam.ac.uk/conts/retrieving.html or from the Director, CCDC, 12 Union Road, Cambridge, CB2, IEZ, UK (fax: +44-1223-336-033; e-mail: deposit@ccdc.cam.ac.uk).

Data availability

Data will be made available on request.

References

[1] J. Pisk, M. Rubčić, D. Kuzman, M. Cindrić, D. Agustin, V. Vrdoljak, Molybdenum(VI) complexes of hemilabile aroylhydrazone ligands as efficient catalysts for greener cyclooctene epoxidation: an experimental and theoretical approach, New J. Chem. 43 (2019) 5531–5542, https://doi.org/10.1039/C9NJ00229D.
[2] R.M. Beteck, R. Seldon, A. Jordaan, D.F. Warner, H.C. Hoppe, D. Laming, L. J. Legoabe, S.D. Khanye, Quinolone-isoniazid hybrids: synthesis and preliminary in vitro cytotoxicity and anti-tuberculosis evaluation, MedChemComm. 10 (2019) 326–331, https://doi.org/10.1039/C8MD00480C.
[3] A.K. Patel, R.N. Jadeja, N. Patel, R.N. Patel, S.K. Patel, Ray.J. Butcher, S. Kumar, G. Kumar, Copper(II) hydrazone complexes derived from (Z)-N′-{(2-hydroxynapthalen-1-yl}methylene)acetohydrazide: synthesis, spectral characterization, electrochemical behaviour, density functional study, in vitro catalytic activity and molecular docking, Results Chem. 4 (2022) 100244, https://doi.org/10.1016/j.rechem.2021.100244.
[4] S. Abbas, M.Mehmood Imtiaz-ud-Din, M.K. Rauf, S.S. Azam, I. Haq, M.N. Tahir, N. Parvaiz, Synthesis, structural characterization, and molecular docking studies of bioactive bismuth(III) complexes with substituted hydrazones, J. Mol. Struct. 1230 (2021) 129870, https://doi.org/10.1016/j.molstruc.2021.129870.
[5] C. Anitha, S. Sumathi, P. Tharmaraj, C.D. Sheela, Synthesis, characterization, and biological activity of some transition metal complexes derived from novel Hydrazone Azo Schiff base Ligand, Int. J. Inorg. Chem. 2011 (2011) 1–8, https://doi.org/10.1155/2011/493942.

[6] P. Politzer, J.S. Murray, T. Clark, Halogen bonding and other σ-hole interactions: a perspective, Phys. Chem. Chem. Phys. 15 (2013) 11178, https://doi.org/10.1039/c3cp00054k.

[7] L. Tom, M.R.P. Kurup, A reversible thermo-responsive 2D Zn(II) coordination polymer as a potential self-referenced luminescent thermometer, J. Mater. Chem. C 8 (2020) 2525–2532, https://doi.org/10.1039/C9TC06710H.

[8] M.C. Vineetha, M. Sithambaresan, Y.S. Nair, M.R. Prathapachandra Kurup, Structural investigation of discrete solvent protonated vanadium and other transition metal complexes of N'-[(E)-(3-ethoxy-2-hydroxyphenyl)methylidene] benzohydrazide, synthetic, spectroscopic and cytotoxicity studies, Inorganica Chim. Acta 491 (2019) 93–104, https://doi.org/10.1016/j.ica.2019.03.040.

[9] D.S. Weiss, M. Abkowitz, Advances in organic photoconductor technology, Chem. Rev. 110 (2010) 479–526, https://doi.org/10.1021/cr900173r.

[10] P.H.O. Santiago, M.B. Santiago, C.H.G. Martins, C.C. Gatto, Copper(II) and zinc(II) complexes with Hydrazone: synthesis, crystal structure, Hirshfeld surface and antibacterial activity, Inorganica Chim. Acta 508 (2020) 119632, https://doi.org/10.1016/j.ica.2020.119632.

[11] V. Meenatchi, S. Siva, L. Cheng, Synthesis, crystal growth, spectroscopic characterization, Hirshfeld surface analysis and DFT investigations of novel nonlinear optically active 4-benzoylpyridine-derived hydrazone, J. Mol. Struct. 1243 (2021) 130858, https://doi.org/10.1016/j.molstruc.2021.130858.

[12] P. Karuppusamy, S. Sarveswari, A 4-phenyl thiophene appended 2,4-dinitrophenylhydrazone as a colorimetric chemosensor for selective detection of cyanide ion and its application for real-life samples, J. Mol. Struct. 1248 (2022) 131494, https://doi.org/10.1016/j.molstruc.2021.131494.

[13] S. Rollas, S.G. Küçükgüzel, Biological activities of hydrazone derivatives, Molecules 12 (2007) 1910–1939, https://doi.org/10.3390/12081910.

[14] R.M. Mohareb, J. Schatz, Anti-tumor and anti-leishmanial evaluations of 1,3,4-oxadiazine, pyran derivatives derived from cross-coupling reactions of β-bromo-6H-1,3,4-oxadiazine derivatives, Bioorg. Med. Chem. 19 (2011) 2707–2713, https://doi.org/10.1016/j.bmc.2011.02.051.

[15] S. Narayanan, P. Gupta, U. Nazim, M. Ali, N. Karadkhelkar, M. Ahmad, Z.-S. Chen, Anti-cancer effect of Indanone-based thiazolyl hydrazone derivative on colon cancer cell lines, Int. J. Biochem. Cell Biol. 110 (2019) 21–28, https://doi.org/10.1016/j.biocel.2019.02.004.

[16] M. Karnatak, M. Hassam, A.S. Singh, D.K. Yadav, C. Singh, Sunil.K. Puri, V. P. Verma, Novel hydrazone derivatives of N-amino-11-azaartemisinin with high order of antimalarial activity against multidrug-resistant Plasmodium yoelii nigeriensis in Swiss mice via intramuscular route, Bioorg. Med. Chem. Lett. 58 (2022) 128522, https://doi.org/10.1016/j.bmcl.2021.128522.

[17] M. Sengupta, A. Guha, R. Bhowmik, I. Kazmi, S.B.I. Hosawi, F. Al-Abbasi, M. Kaleem, Insight into the molecular mechanism of action of anticancer drugs. Synth. Drugs Work, Elsevier, 2023, pp. 477–502, https://doi.org/10.1016/B978-0-323-99855-0.00021-X.

[18] S.S. Sreejith, A. Nair, V.A. Smolenski, J.P. Jasinski, M.R. Prathapachandra Kurup, Cd(II) and Ni(II) complexes from aroyl hydrazones: unravelling the intermolecular interactions and electronic, crystal structures through experimental and theoretical studies, Inorganica Chim. Acta 469 (2018) 264–279, https://doi.org/10.1016/j.ica.2017.09.031.

[19] A. Ajala, A. Uzairu, G.A. Shallangwa, S.E. Abechi, Structure-based drug design of novel piperazine containing hydrazone derivatives as potent alzheimer inhibitors: molecular docking and drug kinetics evaluation, Brain Disord. 7 (2022) 100041, https://doi.org/10.1016/j.dscb.2022.100041.

[20] D. Kuriakose, M.R.P. Kurup, Mononuclear and binuclear dioxidomolybdenum(VI) complexes of ONO appended aroylhydrazone: crystal structures, interaction energy calculation and cytotoxicity, J. Mol. Struct. 1204 (2020) 127467, https://doi.org/10.1016/j.molstruc.2019.127467.

[21] G.M. Sheldrick, SHELXTL Version 5.1, Bruker AXS Inc Madison Wis. USA 53719 (1997).

[22] G. Sheldrick, SADABS, Program for area detector adsorption correction, Inst. Inorg. Chem. Univ. Gött. Ger. 2019 (1996).

[23] SHELXL-97. Program For the Refinement of Crystal Structures; University of Göttingen: Stuttgart, Germany. n.d.

[24] G. Sheldrick, SHELXS-2014, Program For Crystal Structure Solution, Univ. Gottingen, 2014.

[25] W.T. Pennington, *DIAMOND* – Visual crystal structure Information System, J. Appl. Crystallogr. 32 (1999) 1028–1029, https://doi.org/10.1107/S0021889899011486.

[26] Gaussian 09, Revision A.02, M.J. Frisch, G.W. Trucks, H.B. Schlegel, G.E. Scuseria, M.A. Robb, J.R. Cheeseman, G. Scalmani, V. Barone, G.A. Petersson, H. Nakatsuji, X. Li, M. Caricato, A. Marenich, J. Bloino, B.G. Janesko, R. Gomperts, B. Mennucci, H.P. Hratchian, J.V. Ortiz, A.F. Izmaylov, J.L. Sonnenberg, D. Williams-Young, F. Ding, F. Lipparini, F. Egidi, J. Goings, B. Peng, A. Petrone, T. Henderson, D. Ranasinghe, V.G. Zakrzewski, J. Gao, N. Rega, G. Zheng, W. Liang, M. Hada, M. Ehara, K. Toyota, R. Fukuda, J. Hasegawa, M. Ishida, T. Nakajima, Y. Honda, O. Kitao, H. Nakai, T. Vreven, K. Throssell, J.A. Montgomery, Jr., J.E. Peralta, F. Ogliaro, M. Bearpark, J.J. Heyd, E. Brothers, K.N. Kudin, V.N. Staroverov, T. Keith, R. Kobayashi, J. Normand, K. Raghavachari, A. Rendell, J.C. Burant, S.S. Iyengar, J. Tomasi, M. Cossi, J.M. Millam, M. Klene, C. Adamo, R. Cammi, J.W. Ochterski, R.L. Martin, K. Morokuma, O. Farkas, J.B. Foresman, and D.J. Fox, Gaussian, Inc., Wallingford CT, 2016., (n.d.).

[27] W. Kohn, L.J. Sham, Self-consistent equations including exchange and correlation effects, Phys. Rev. 140 (1965) A1133–A1138, https://doi.org/10.1103/PhysRev.140.A1133.

[28] R. Dennington, T.A. Keith, J.M. Millam, GaussView, Version 6.0. 16, 16, Semichem Inc, Shawnee Mission, 2016. Vol.(n.d.).

[29] T. Claridge, Software review of MNova: NMR Data Processing, Analysis, and Prediction Software, J. Chem. Inf. Model. 49 (2009) 1136–1137, https://doi.org/10.1021/ci900090d.

[30] M.J. Turner, S.P. Thomas, M.W. Shi, D. Jayatilaka, M.A. Spackman, Energy frameworks: insights into interaction anisotropy and the mechanical properties of molecular crystals, Chem. Commun. 51 (2015) 3735–3738, https://doi.org/10.1039/C4CC09074H.

[31] P.R. Spackman, M.J. Turner, J.J. McKinnon, S.K. Wolff, D.J. Grimwood, D. Jayatilaka, M.A. Spackman, *CrystalExplorer* : a program for Hirshfeld surface analysis, visualization and quantitative analysis of molecular crystals, J. Appl. Crystallogr. 54 (2021) 1006–1011, https://doi.org/10.1107/S1600576721002910.

[32] E.-M. Ourhzif, I. Abrunhosa-Thomas, P. Chalard, M. Khouili, Y. Troin, M. Akssira, E.M. Ketatni, Synthesis, characterization, crystal structure, Hirshfeld surface analysis and DFT studies of novel compounds based on the methoxynaphthalene ring, J. Mol. Struct. 1244 (2021) 130947, https://doi.org/10.1016/j.molstruc.2021.130947.

[33] K. Jayasheela, L.H. Al-Wahaibi, S. Periandy, H.M. Hassan, S. Sebastian, S. Xavier, J. C. Daniel, A.A. El-Emam, M.I. Attia, Probing vibrational activities, electronic properties, molecular docking and Hirshfeld surfaces analysis of 4-chlorophenyl ({[(1E)-3-(1H-imidazol-1-yl)-1-phenylpropylidene]amino}oxy)methanone: a promising anti-Candida agent, J. Mol. Struct. 1159 (2018) 83–95, https://doi.org/10.1016/j.molstruc.2018.01.042.

[34] L. El Foujji, K. El Bourakadi, E.M. Essassi, R.T. Boeré, A.E.K. Qaiss, R. Bouhfid, Solid-state zwitterionic tautomerization of 2-((5-methyl-1H-pyrazol-3-yl)methyl)-1H-benzimidazole: synthesis, characterization, DFT calculation and docking studies, J. Mol. Struct. 1235 (2021) 130231, https://doi.org/10.1016/j.molstruc.2021.130231.

[35] L.A. Anthony, D. Rajaraman, G. Sundararajan, M. Suresh, P. Nethaji, R. Jaganathan, K. Poomani, Synthesis, crystal structure, Hirshfeld surface analysis, DFT, molecular docking and molecular dynamic simulation studies of (E)-2,6-bis (4-chlorophenyl)-3-methyl-4-(2-(2,4,6-trichlorophenyl)hydrazono)piperidine derivatives, J. Mol. Struct. 1266 (2022) 133483, https://doi.org/10.1016/j.molstruc.2022.133483.

[36] J.R. Donaldson, S.L. Warner, R.G. Cates, D.Gary Young, Assessment of antimicrobial activity of fourteen essential oils when using dilution and diffusion methods, Pharm. Biol. 43 (2005) 687–695, https://doi.org/10.1080/13880200500384932.

[37] Y. Zhang, Z. Liu, T. Shan, Y. Wang, L. Zhu, T. Li, F. Liu, H. Zhong, Tuning the molecular geometry and packing mode of non-fullerene acceptors by altering the bridge atoms towards efficient organic solar cells, Mater. Chem. Front. 4 (2020) 2462–2471, https://doi.org/10.1039/D0QM00277A.

[38] C.F. Macrae, P.R. Edgington, P. McCabe, E. Pidcock, G.P. Shields, R. Taylor, M. Towler, J. Van De Streek, *Mercury* : visualization and analysis of crystal structures, J. Appl. Crystallogr. 39 (2006) 453–457, https://doi.org/10.1107/S002188980600731X.

[39] Biovia, D.S. (2019) Discovery Studio Visualizer. San Diego., (n.d.).

[40] Y. Liu, M. Grimm, W. Dai, M. Hou, Z.-X. Xiao, Y. Cao, CB-Dock: a web server for cavity detection-guided protein–ligand blind docking, Acta Pharmacol. Sin. 41 (2020) 138–144, https://doi.org/10.1038/s41401-019-0228-6.

[41] R. Datta, V. Ramya, M. Sithambaresan, M.R.P. Kurup, Crystal structure of 4-{(*E*)-[2-(pyridin-4-ylcarbonyl)hydrazin-1-ylidene]methyl}phenyl acetate monohydrate, Acta Crystallogr. Sect. E Crystallogr. Commun. 71 (2015) o79, https://doi.org/10.1107/S2056989014027819. –o80.

[42] Md.H.A. Banna, Md.C. Sheikh, R. Miyatake, Md.B.H. Howlader, E. Zangrando, Crystal structure of 4-[(4-methylbenzyl)oxy]- *N* ′-(4-nitrobenzylidene) benzohydrazide: a new hydrazone derivative, Acta Crystallogr. Sect. E Crystallogr. Commun 79 (2023) 531–533, https://doi.org/10.1107/S2056989023003948.

[43] C. Cui, Q. Meng, Y. Wang, *N* ′-[4-(Dimethylamino)benzylidene]benzohydrazide, Acta Crystallogr. Sect. E Struct. Rep. Online 65 (2009) o2472, https://doi.org/10.1107/S1600536809036460. –o2472.

[44] F. Su, Z.-G. Gu, J. Lin, 4-Dimethylamino- *N* ′-(2-methoxybenzylidene) benzohydrazide, Acta Crystallogr. Sect. E Struct. Rep. Online 67 (2011) o1896, https://doi.org/10.1107/S1600536811025220. –o1896.

[45] X. Zhang, X. Fu, L. Tan, C. Wang, W. Fan, 4-Dimethylamino- *N* ′-(4-nitrobenzylidene)benzohydrazide methanol monosolvate, Acta Crystallogr. Sect. E Struct. Rep. Online 68 (2012) o2828, https://doi.org/10.1107/S1600536812037063. –o2828.

[46] B. Joseph, N.R. Sajitha, M. Sithambaresan, E.B. Seena, M.R.P. Kurup, Crystal structure of *N* ′-[(*E*)-3,5-dichloro-2-hydroxybenzylidene]-4-nitrobenzohydrazide dimethylformamide monosolvate, Acta Crystallogr. Sect. E Crystallogr. Commun 71 (2015) o826, https://doi.org/10.1107/S2056989015018290. –o827.

[47] M. Srnec, E.I. Solomon, Frontier Molecular Orbital contributions to chlorination versus hydroxylation selectivity in the non-heme iron halogenase SyrB2, J. Am. Chem. Soc. 139 (2017) 2396–2407, https://doi.org/10.1021/jacs.6b11995.

[48] S. Soleimani Amiri, S. Makarem, H. Ahmar, S. Ashenagar, Theoretical studies and spectroscopic characterization of novel 4-methyl-5-((5-phenyl-1,3,4-oxadiazol-2-yl)thio)benzene-1,2-diol, J. Mol. Struct. 1119 (2016) 18–24, https://doi.org/10.1016/j.molstruc.2016.04.053.

[49] A.J. Garza, O.I. Osman, N.A. Wazzan, S.B. Khan, A.M. Asiri, G.E. Scuseria, A computational study of the nonlinear optical properties of carbazole derivatives: theory refines experiment, Theor. Chem. Acc. 133 (2014) 1458, https://doi.org/10.1007/s00214-014-1458-9.

[50] M.R.S.A. Janjua, Z.H. Yamani, S. Jamil, A. Mahmood, I. Ahmad, M. Haroon, M. H. Tahir, Z. Yang, S. Pan, First principle study of electronic and non-linear optical (NLO) properties of triphenylamine dyes: interactive design computation of new

NLO compounds, Aust. J. Chem. 69 (2016) 467–472, https://doi.org/10.1071/CH15402.
[51] S.M. Sana Mazhar, M.K. Muhammad Khalid, M.N.T. Muhammad Nawaz Tahir, M. H. Muhammad Haroon, T.A. Tashfeen Akhtar, M.U.K. Muhammad Usman Khan, F. J. Farrukh Jaleel, M.A. Muhammad Aslam, Facile synthesis, crystal growth, quantum chemical studies of electronic structure and of the profoundly persuasive NLO organic crystal: ethyl 4-[N,N-bis(p-toluenesulfonyl)]- aminobenzoate, J. Chem. Soc. Pak. 41 (2019) 122, https://doi.org/10.52568/000713/JCSP/41.01.2019. –122.
[52] R.G. Parr, R.A. Donnelly, M. Levy, W.E. Palke, Electronegativity: the density functional viewpoint, J. Chem. Phys. 68 (1978) 3801–3807, https://doi.org/10.1063/1.436185.
[53] R.G. Parr, L.V. Szentpály, S. Liu, Electrophilicity Index, J. Am. Chem. Soc. 121 (1999) 1922–1924, https://doi.org/10.1021/ja983494x.
[54] Mohd. Shkir, P.S. Patil, M. Arora, S. AlFaify, H. Algarni, An experimental and theoretical study on a novel donor-π-acceptor bridge type 2, 4, 5-trimethoxy-4′-chlorochalcone for optoelectronic applications: a dual approach, Spectrochim. Acta. A. Mol. Biomol. Spectrosc. 173 (2017) 445–456, https://doi.org/10.1016/j.saa.2016.09.022.
[55] R. PR, L. Tom, D. NP, K.P. Safna Hussan, V.P. Raphael, V.B. Bhagyesh, B. Joseph, Two novel aroyl hydrazones from 4-methoxybenzhydrazide: comprehensive study including synthesis, X-ray crystallography, DFT analysis, antibacterial activity and molecular docking, J. Mol. Struct. 1335 (2025) 141866, https://doi.org/10.1016/j.molstruc.2025.141866.
[56] S. Naseem, M. Khalid, M.N. Tahir, M.A. Halim, A.A.C. Braga, M.M. Naseer, Z. Shafiq, Synthesis, structural, DFT studies, docking and antibacterial activity of a xanthene based hydrazone ligand, J. Mol. Struct. 1143 (2017) 235–244, https://doi.org/10.1016/j.molstruc.2017.04.093.
[57] G. Xu, B. Tang, L. Gu, P. Zhou, H. Li, Open coordination sites-induced structural diversity of a new series of Cu(II) complexes with tridentate aroylhydrazone Schiff base, J. Mol. Struct. 1120 (2016) 205–214, https://doi.org/10.1016/j.molstruc.2016.05.034.
[58] K. Chandrasekaran, R.Thilak Kumar, Structural, spectral, thermodynamical, NLO, HOMO, LUMO and NBO analysis of fluconazole, Spectrochim. Acta. A. Mol. Biomol. Spectrosc. 150 (2015) 974–991, https://doi.org/10.1016/j.saa.2015.06.018.
[59] K. Singh, I. Bala, R. Kataria, Crystal structure, Hirshfeld surface and DFT based NBO, NLO, ECT and MEP of benzothiazole based hydrazone, Chem. Phys. 538 (2020) 110873, https://doi.org/10.1016/j.chemphys.2020.110873.
[60] J. Petit, N. Meurice, C. Kaiser, G. Maggiora, Softening the rule of five—Where to draw the line? Bioorg. Med. Chem. 20 (2012) 5343–5351, https://doi.org/10.1016/j.bmc.2011.11.064.